Remote Sensing of Environment 299 (2023) 113852

Contents lists available at ScienceDirect

Remote Sensing of Environment

journal homepage: www.elsevier.com/locate/rse

A method for continuous sub-annual mapping of forest disturbances using optical time series

Daniele Marinelli [a,*], Michele Dalponte [a], Lorenzo Frizzera [a], Erik Næsset [b], Damiano Gianelle [a]

[a] Forest Ecology Unit, Research and Innovation Centre, Fondazione Edmund Mach, Via Edmund Mach, 1, San Michele All'adige, 38098, Italy
[b] Faculty of Environmental Sciences and Natural Resource Management, Norwegian University of Life Sciences, P.O. Box 5003, Ås, NO-1432, Norway

ARTICLE INFO

Edited by Marie Weiss

Dataset link: doi.org/10.5281/zenodo.8426109

Keywords:
Forest disturbances
Time series
Sentinel-2
Change detection
Bark beetle

ABSTRACT

Forest disturbances have a major impact on ecosystem dynamics both at local and global scales. Accordingly, it is important to acquire objective information about the location, nature and timing of such events to improve the understanding of their impact, update forest management policies and disturbance mitigation strategies. To this date, remotely sensed data have been widely used for the detection of stand replacing disturbances (SRD) such as windthrows and wildfires. In contrast, less effort has been devoted to the detection of non-stand replacing disturbances (NSRD), typically characterized by slower and gradual temporal dynamics. To address this gap, we propose a method for the automated detection of both SRD and NSRD. The proposed method can detect both past and recent disturbances, with a monthly temporal resolution, in a near real-time fashion by processing new images as they are acquired. Differently from existing approaches that handle the time series as a one-dimensional (1D) temporal trajectory, the method analyzes the sequence of images by organizing them in a two-dimensional (2D) grid-like structure. This representation allows us to model both the intra- and inter-annual variations of the time series taking advantage of the annual cyclical nature of the plant phenology. The method has been tested on study areas attacked by bark beetles achieving a user's accuracy and producer's accuracy of 0.91±0.08 and 0.81±0.07 (with 95% confidence intervals) for the disturbed areas, respectively.

1. Introduction

Forests are continuously affected by changes that can be grouped under the umbrella term of forest disturbances. Locally, disturbances affect both the environment and the social and economic spheres (Hlásny et al., 2019; Brecka et al., 2018). In terms of global scale effects, disturbances affect the carbon flux between the biosphere and the atmosphere (Hirsch et al., 2004; Kurz et al., 2008). In recent years, the frequency and severity of disturbances have increased (Seidl et al., 2017) with climate change likely being one of the drivers of such increment (Seidl et al., 2011; Senf and Seidl, 2021). Therefore, it is important to gather objective information regarding the nature, location and extent of forest disturbances (Tyukavina et al., 2017) to estimate damages, define possible mitigation strategies and update management policies. On a larger scale, modeling disturbances is important to estimate their effect on carbon fluxes (Liu et al., 2011; Gong et al., 2022) in the context of carbon accounting programs (Kurz et al., 2009; Waterworth and Richards, 2008).

Remote sensing is an ideal technology for forest disturbances monitoring. In the past, due to data scarcity and accessibility related both to costs and technical limitations (Turner et al., 2015), most approaches for forest disturbance detection were based on change detection methods that use pairs or few images (Coops et al., 2007; Frolking et al., 2009). In recent years, the open data policies for archives (e.g., Landsat archive) and new data sources (e.g., ESA Sentinel program) considerably increased the data availability. This has led to an increased interest in multitemporal information analysis (Bovolo and Bruzzone, 2015) applied to forestry applications (Wulder et al., 2019). In this regard, several methods exploit time series for forest disturbance detection, especially considering archival datasets such as Landsat (Kennedy et al., 2010; Zhu and Woodcock, 2014; Hermosilla et al., 2015; Giannetti et al., 2020). Most of these approaches use annual composites generated using different approaches (White et al., 2014) which however strongly limit the temporal resolution of the detection. Other studies (Zhu and Woodcock, 2014) exploit all the available images to explore seasonal trends using sinusoidal time series models enabling the near real-time disturbance detection at sub-annual temporal resolution.

When considering near real-time disturbance detection, the S2 constellation can potentially be a superior open data source compared to Landsat (Lima et al., 2019) due to the shorter revisit time (up to two-three days at mid latitudes) and smaller pixel spacing (up to

* Corresponding author.
E-mail address: daniele.marinelli@fmach.it (D. Marinelli).

https://doi.org/10.1016/j.rse.2023.113852
Received 6 July 2023; Received in revised form 4 October 2023; Accepted 8 October 2023
Available online 13 October 2023
0034-4257/© 2023 The Author(s). Published by Elsevier Inc. This is an open access article under the CC BY-NC-ND license (http://creativecommons.org/licenses/by-nc-nd/4.0/).

10 m). In particular, the S2 spatial resolution allows for the detection of smaller patches of disturbances and it is more suited to the fragmented forests of central and southern Europe. Moreover, the shorter revisit time is suited for a continuous monitoring (Mulverhill et al., 2023) at sub-annual scale. Several methods for forest disturbance detection with S2 images have been developed (Löw and Koukal, 2020; Francini et al., 2021; Huo et al., 2021), including some using both S2 and Landsat data (Zanetti et al., 2022; Zhang et al., 2021). In this regard, great interest has been devoted to the harmonized Landsat Sentinel (HLS) dataset which provides a collection of Landsat and S2 harmonized images (Claverie et al., 2018; Mulverhill et al., 2023).

While several approaches can detect non-stand replacing disturbances (NSRD), most of the effort has been devoted to stand replacing disturbances (SRD). This is due to both design choices and the greater availability of SRD reference data that make them a favored choice for validation (Coops et al., 2020). SRD have very distinctive spectral signature dynamics and spatial patterns associated with a clear change of land cover. Therefore, SRD can be easily separated from natural amplitude variations associated with the phenological cycle (Coops et al., 2007). In contrast, NSRD exhibit gradual and small magnitude variations, with varying degrees of impact on forests (Coops et al., 2020). This characteristic increases the difficulty of discriminating true NSRD from noise and natural phenological oscillations (Gao et al., 2020). Accordingly, there is the need of methods that exploit the high revisit frequency of satellites constellation (e.g., S2) to model vegetation dynamics to detect NSRD. In particular, it is important to consider the annual/seasonal repetitive nature of the time series associated with the phenological cycle. This can be taken into account fitting temporal trajectories that model the cyclical nature (e.g., sinusoidal curve). However, the fitting can require very long time series to reliably estimate the model parameters (Francini et al., 2022), it may overfit in the case of missing data and it can be a computationally intensive operation (Zhu and Woodcock, 2014).

The aim of this paper is to address these challenges by developing and validating a method for the automated detection of SRD and NSRD using multi-year optical time series. The method is based on a representation of the sequence of images in a grid-like structure (Bruzzone and Bovolo, 2014; Bertoluzza et al., 2017) that enables the analysis of the time series in a 2D domain representing both the intra- and inter-annual variations. This representation exploits the annual cyclical nature of plants to reduce the impact of phenology and analyzes both variations (i.e., both directions of the 2D grid) to increase the sensitivity to subtle NSRD. Moreover, by analyzing also the intra-annual variations, the method can perform the monitoring at sub-annual scale, processing new images as they are acquired, thus improving the temporal resolution (i.e., monthly) as opposed to methods based only on annual images (Hermosilla et al., 2015; Francini et al., 2021).

2. Materials

2.1. Study area

The study area covers the entire forested area (390 000 ha) of the province of Trento, Italy, located in the Southern Alps (Fig. 1(a)). It is characterized by a very complex and heterogeneous terrain morphology with altitudes ranging from 65 to 3764 m above sea level. In terms of species composition, 67% of the forests are conifers dominated, i.e., Silver fir (*Abies alba* Mill.), Norway spruce (*Picea abies* (L.) Karst.), European larch (*Larix decidua* Mill.), Austrian pine (*Pinus nigra* J.F.Arnold) and Scots pine (*Pinus sylvestris* L.), with the remaining 33% being composed by broadleaves including European beech (*Fagus sylvatica* L.), Hop hornbeam (*Ostrya carpinifolia* Scop.), oaks (*Quercus sp.*) and maples (*Acer sp.*) (Rodeghiero et al., 2010).

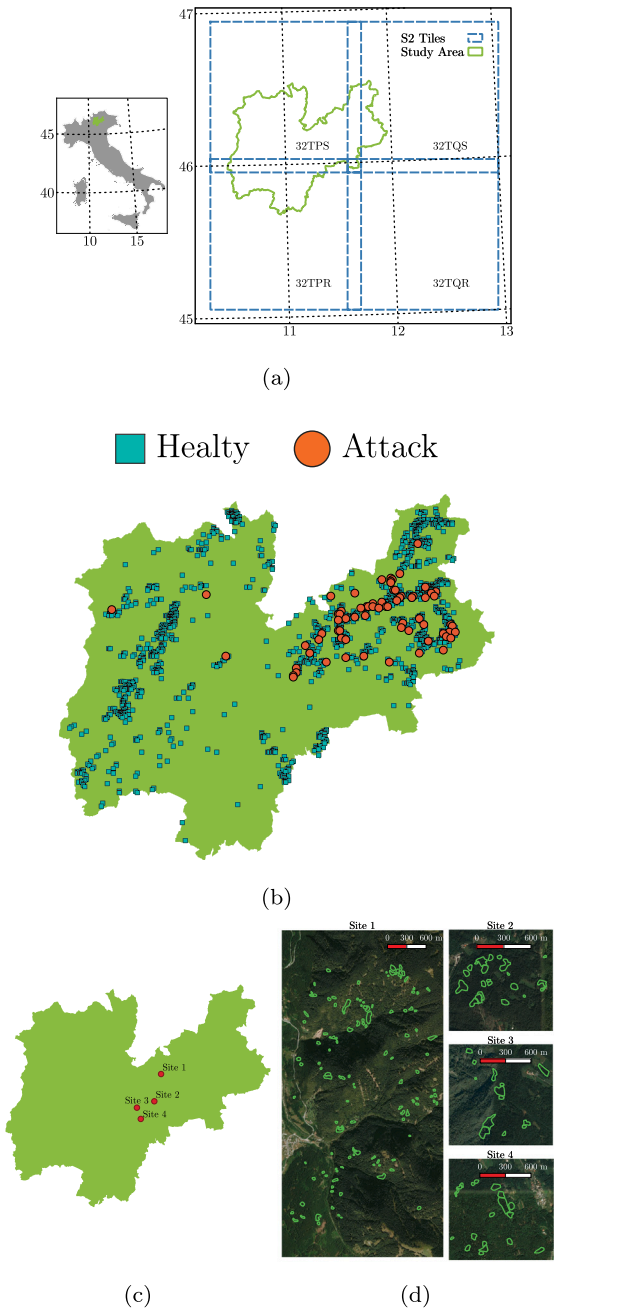

Fig. 1. Dataset overview: (a) Location of the province of Trento (in green) with the S2 tiles in blue. (b) Position of the point-based dataset with the sample units labeled as attacked showed as orange circles. (c–d) Location and detail of the four study sites of the polygon-based dataset. (For interpretation of the references to color in this figure legend, the reader is referred to the web version of this article.)

2.2. Reference data

To evaluate the performances of the proposed method, we examined the NSRD related to the infestation of the Norway spruce bark beetle (*Ips typographus* L.), which spread following the Vaia storm that struck the North East of Italy in October 2018 (Giovannini et al., 2021). Two reference datasets were created by photointerpretation of Planet basemaps (PB) monthly composites (Planet Team, 2017–), which were derived from images captured by the PlanetScope constellation between June 2018 and August 2022. The photointerpretation was carried out by three interpreters, including two remote sensing experts

and a forester, to ensure independent evaluations and avoid decision ties (McRoberts et al., 2018). The first dataset is point-based and serves to provide a quantitative validation of the method's performance. The second dataset is polygon-based and aims at providing a qualitative evaluation from an operational point of view.

2.2.1. Point-based dataset

The aim of the point-based dataset is to provide a statistically rigorous accuracy assessment. It was therefore designed and collected as a probability sample of points. First, to ensure adequate spatial coverage of the study area (see Fig. 1(b)) while limiting the amount of manual analysis required (Olofsson et al., 2014), we chose to focus exclusively on areas dominated by Norway spruce, which is the species attacked by bark beetle. This was done also since no fine spatial detail tree species map is available making it impossible to select all Norway spruce areas. Consequently, we used a forest inventory map of the province of Trento that defines the tree species composition, in terms of proportion, of each parcel. We selected all the forest parcels with at least 95% of Norway spruce (i.e., ≈26 000 ha of the total 130 000 ha of Norway spruce in the province). Although this is a map which is regularly updated by the forest service and assumed to have only small errors, no data regarding map accuracy are available. At least some minor errors should be expected. The statistical analysis of the point dataset was therefore conditional on the selected area. Thus, the Norway spruce dominated area was our sampling frame and in the statistical analysis it was assumed to be defined without error. Note that an implication of this assumption is that the results will be valid only for the sampled area. The parcels were systematically sampled using a uniformly spaced grid of points every 400 m. Each point was independently inspected by the three interpreters and classified as either attacked or healthy. Despite the photointerpretation process being independent, the interpreters maintained continuous communication to address and discuss challenging cases. The resulting classifications were combined using a majority rule approach, which yielded 1278 (94.7%) healthy points and 71 (5.3%) attacked points. Fig. 1(b) shows the sample distribution with most of the outbreaks concentrated in the northeastern portion of the province.

2.2.2. Polygon-based dataset

The polygon-based dataset was developed to evaluate the method's performance in detecting individual outbreaks and determining the timeliness of detection compared to manual photointerpretation. These aspects are crucial from the forest practitioners perspective, as they offer a measure of the method's effectiveness in real-world scenarios. We selected four study sites (Fig. 1(c)) covering a total area of 1600 ha, each with distinct terrain morphology characteristics. Please note that although these study sites are not representative of the entire study area, they are situated in its northeastern part, which has been the most severely affected by outbreaks. The manual delineation process was conducted as follows: (1) one interpreter delineated all polygons, (2) the other two interpreters reviewed the reference data to add any missing polygons and update polygon boundaries, and (3) each polygon was assigned the earliest date (year and month) when the attack was detectable in the PB. The delineation activity resulted in 194 polygons with a minimum, maximum and average area of 0.02, 1.36 and 0.22 ha, respectively (Fig. 1(d)). These statistics highlight the more fragmented nature of forest disturbances in the Alps compared to other ecosystems (Hermosilla et al., 2019). Finally, randomly sampled healthy forest areas were used to create 63 polygons for comparison with attacked areas.

2.3. Multispectral satellite imagery

The optical images were acquired by the S2 constellation from June 2018 to August 2022. Although S2 imagery was chosen as the primary data source for this study due to the advantages discussed in Section 1, it is worth noting that other data sources, such as Landsat or Planet, can also be used. We considered the months from June to October for each year for a total of 857 images split across four S2 tiles: (1) T32TPR (288 images), (2) T32TPS (287 images), (3) T32TQR (141 images) and (4) T32TQS (141 images). The rationale of using mainly summer and early autumn images was to avoid false positives due to snow or the effects of large variations in the start and end dates of the growing season. Moreover, in temperate climates most of the changes associated to NSRD occur during the growing season (Coops et al., 2006). All images were processed with sen2cor to level 2A, i.e, bottom of atmosphere (BOA). Cloud masking was applied with the s2cloudless algorithm (Skakun et al., 2022) (with cloud probability threshold set to 0.2). Finally, the Scene Classification Map provided by the LA processing was used to discard all the areas of no interest (e.g., snow and water pixels).

3. Methods

The proposed method comprises two main parts: (1) generating temporally spaced composites to enable uniform comparisons across different years, and, (2) performing a grid-based time series analysis to detect variations associated with forest disturbances.

3.1. Monthly composites generation

To detect disturbances, we analyze the time series searching for deviations in the phenological trajectory of a vegetation index (i.e., spectral index). Note that also one or multiple spectral bands can be employed. Let $\mathbf{I} = \{I_t\}_{t=1}^{N}$ be the time series of N images where t is the acquisition date.

The proposed method analyzes the multi-year time series by performing comparisons across multiple years (i.e., inter-annual analysis). To this end, we compute composites obtaining a fixed number of images per year, thus strongly simplifying the inter-annual analysis. Composites have several advantages (Paris et al., 2020) and have been widely used in the detection of disturbances (Hermosilla et al., 2019; Giannetti et al., 2020) and other forest changes such as afforestation (Cavalli et al., 2023; Francini et al., 2023). However, these methods mainly use annual composites limiting the temporal resolution of the detection. In order to monitor intra-annual (i.e., within the individual year) variations, we must consider sub-annual composites. Accordingly, we select a monthly time span for each composite given the temporal dynamics of NSRD and the revisit frequency of the S2 constellation. Compared to existing methods that update the disturbances map yearly, the use of monthly composites substantially improve the temporal resolution of the method. Let us focus on the images acquired during month m and year y, i.e., the images for which $t^s_{y,m} \le t \le t^e_{y,m}$ where $t^s_{y,m}$ and $t^e_{y,m}$ are the start and end dates of the month. The composite image $X_{y,m}$ is generated working pixel-by-pixel and collapsing all the values of the pixel into one according to a median operator $\mathcal{M}$:

$$X_{y,m} = \mathcal{M}\left(\left\{ I_t | t^s_{y,m} \le t \le t^e_{y,m} \right\}\right). \quad (1)$$

The result is a time series of monthly composites $\mathbf{X} = \{X_{y,m}\}$, $(Y^s \le y \le Y^e, 6 \le m \le 10)$ where Y^s and Y^e are the first and last year of the time series, respectively, and m ranges from the 6th (i.e., June) to the 10th (i.e., October) month of the year. The values of masked pixels (e.g., due to clouds) are computed as the average of the previous and following composites or by using the nearest available composite if the same pixel is masked for more consecutive months.

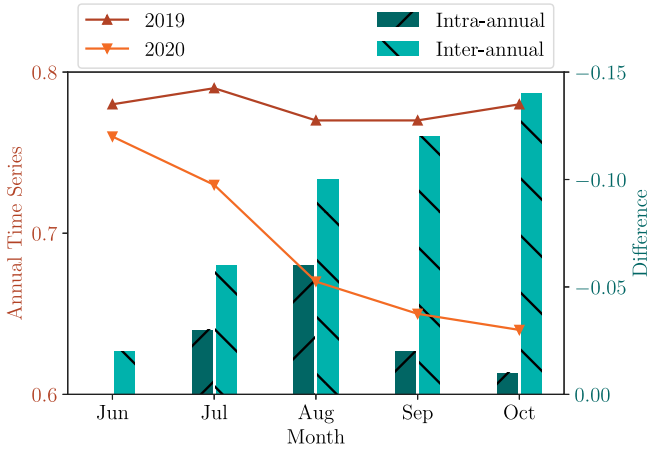

Fig. 2. Example of temporal vegetation index profiles showing on the left Y-axis (warm colors) the temporal trajectories of two consecutive years with a bark beetle attack starting at the beginning of the summer of 2020. The right Y-axis (cold colors) shows the values of the difference between adjacent months (intra-annual) for the 2020 trajectory and between the 2020 and 2019 series (inter-annual). The right Y-axis is inverted.

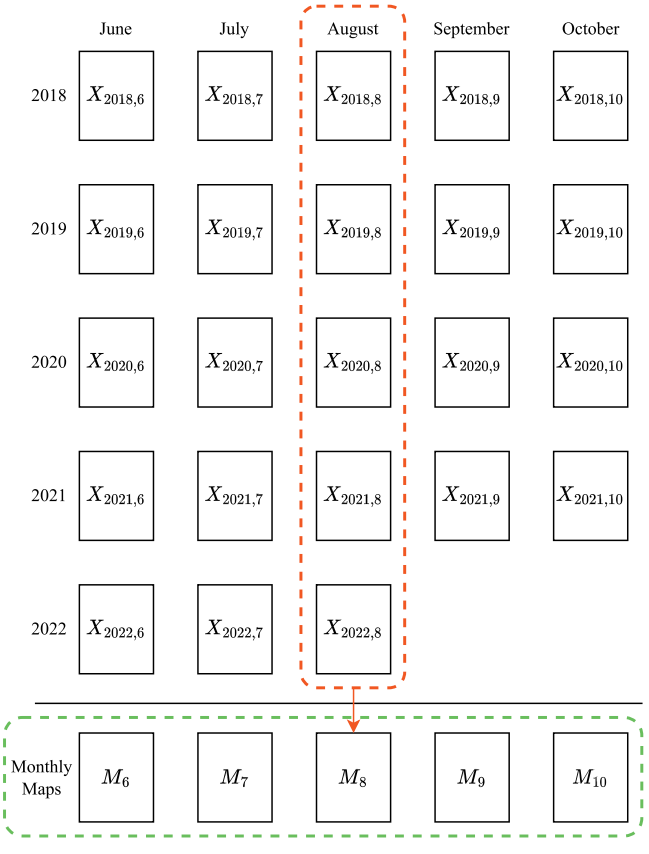

Fig. 3. Monthly composites time series (from June to October and from 2018 to 2022) represented in a grid format (rows correspond to years and columns to months). Each position in the grid represents a monthly composite. The red dashed rectangle shows an example of inter-annual analysis for one month (i.e., August). The green dashed rectangle shows the monthly maps **M** (result of the inter-annual analysis) that are analyzed by the intra-annual analysis.

3.2. Time series analysis

In the second part, we explore the monthly composites time series **X** searching for changes in the spectral index that can be attributed to disturbances. To ensure applicability across the entire study area, the method must be able to handle complex scenarios without relying on condition-dependent parameters. However, detecting changes in **X** between adjacent months (e.g., by computing the difference between $X_{2020,6}$ and $X_{2020,7}$) is strongly influenced by the speed and severity of the disturbance, that may vary across space. In the case of NSRD, Fig. 2 shows that when considering short time spans, only a small variation of the spectral index can be seen. Furthermore, following a substantial impact observed during the initial phase (Coops et al., 2020), the magnitude of variation gradually diminishes as the attack approaches its conclusion. Consequently, if the disturbance goes undetected during the phase of largest magnitude, it is very likely that the intra-annual analysis will fail to identify it. To address this issue, we investigate the information content of **X** using both intra-annual and inter-annual (e.g., $X_{2020,7}$, $X_{2021,7}, \dots$) analyses. This can be visually represented by organizing the composites in a grid representation where each composite is assigned to a position defined by two coordinates, i.e.,:

$$\begin{bmatrix} X_{2018,6} & X_{2018,7} & \cdots & X_{2018,10} \\ \vdots & \vdots & \ddots & \vdots \\ X_{2020,6} & X_{2020,7} & \cdots & X_{2020,10} \\ \vdots & \vdots & \ddots & \vdots \\ X_{2022,6} & X_{2022,7} & X_{2022,8} & \end{bmatrix} \tag{2}$$

According to this representation, shown in Fig. 3, we can perform the analysis both in the vertical direction (inter-annual analysis) and in the horizontal direction (intra-annual analysis).

3.2.1. Inter-annual analysis

First, we analyze each month individually comparing the values of the composites across the different years. In this way we exploit the annual cyclical nature of the dynamics of trees by comparing composites that correspond to the same time of the year, and therefore phenological phase, thus neutralizing or reducing its effects on the disturbance detection. This has two additional advantages. Firstly, in the case of disturbances, the difference computed over this interval tends to have larger absolute values than when computed over a shorter period, also for NSRD. Secondly, as the spectral values decrease compared to the previous year, the difference becomes more pronounced over time, as the changes from previous months accumulate (as shown by the light cyan bars in Fig. 2). An extended comparison between inter- and intra-annual analysis is presented in the Results and Discussion sections.

Let us consider a generic month m' and the subset of composites $\mathbf{X}_{m'} = \left\{X_{y,m=m'}\right\}, (Y^s \le y \le Y^e)$. First, we compute the set of backward differences $\mathbf{X}^{BD} = \left\{X^{BD}_{y,m'}\right\}, ((Y^s+1) \le y \le Y^e)$ at the pixel level, where $X^{BD}_{y,m'} = X_{y,m'} - X_{y-1,m'}$. We then identify the first year y_f that exhibits a negative variation in the spectral index, compared to the previous year, with an absolute value greater than a threshold TH. Such a negative variation can be indicative of a disturbance.

Year $y_f - 1$ is the last one before the vegetation index drops and $X_{y_f-1,m'}$ can be considered as a reference value in pre-disturbance conditions. We use this value to compute $\mathbf{X}^{RD} = \left\{X^{RD}_{y,m'}\right\}, \left(y_f \le y \le Y^e\right)$, where $X^{RD}_{y,m'} = X_{y,m'} - X_{y_f-1,m'}$ represents the vegetation index variation from the reference year $y_f - 1$. It is reasonable to expect that after most disturbances, the vegetation index values will remain anomalously small for several years. Five years is a typical temporal range used to check for recovery after the disturbance event (Kennedy et al., 2012; White et al., 2017; Hermosilla et al., 2019) in temperate climates. Accordingly, we consider as disturbed areas only the pixels that show a negative variation of the index from the reference year for at least three

Table 1
Set of rules for the detection reliability.

Level	Rule
Low	Detection for one month
Medium	Detection for two months in the same year
High	Detection for more than two months or two different years

years. Given the first year of detection y_d, the pixel is considered as disturbed if $X^{RD}_{y,m'} \leq TH \; \forall \; y_d \leq y \leq y_d+3$. Note that if $Y^e - y_d < 3$, i.e., if the number of years available in the time series after the first detection is less than three, or zero in the case of near real-time detection, the condition is still considered fulfilled. The analysis results in a map $M_{m'}$ in which each pixel represents the first year y_d of detection or zero otherwise. By applying the inter-annual analysis to each month, we obtain the set of maps $\mathbf{M} = \{M_m\}$, $6 \leq m \leq 10$.

3.2.2. Intra-annual analysis

In this second part, we analyze set **M** at the pixel level searching for temporal inconsistencies to reduce the false positives. In particular, we consider two assumptions:

Temporal Continuity If a disturbance is detected at a given month m', all the following months should also show a detection, i.e.,:

$$M_{m'} > 0 \iff M_m > 0, \; \forall \; m > m'. \tag{3}$$

Temporal Order If a disturbance is detected at a given month m' at a given year, the year of detection of the following months should be equal to or smaller than the first one, i.e.,

$$M_{m'} > 0 \iff M_{m'} \geq M_m, \; \forall \; m > m'. \tag{4}$$

These assumptions are based on the prolonged and continuous impact in time of disturbances which should be reflected in the maps of **M**.

We estimate the first year (Fig. 4) and month of detection for each pixel in the set **M** and compute a detection reliability metric based on three levels. The three levels are based on how long the candidate disturbance has been detected, as shown in Table 1. The reliability metric is important because the method processes new images as they are acquired, which increases sensitivity to fluctuations in the time series that are not associated with phenological deviations (e.g., atmospheric haze) and can lead to false positives. Since false positives cannot be removed until at least one new composite is generated and processed, this metric helps evaluate the detection reliability from an operational point of view.

3.3. Experimental setup

3.3.1. Spectral indices

We tested four indices commonly used for disturbance detection, namely the NDVI, modified soil adjusted vegetation index 2 (MSAVI2), normalized burned ratio (NBR) and normalized difference red edge (NDRE) (Verbesselt et al., 2010; Matricardi et al., 2013; Hermosilla et al., 2015; Eitel et al., 2011). This is to analyze the impact of different spectral bands such as near-infrared (NIR), short wave infrared (SWIR) and red edge, on the method performances. To assess the sensitivity of the method to the threshold parameter, we considered different values of TH, specifically $TH = \{-0.05, -0.1, -0.2\}$.

3.3.2. Evaluation strategies

The quantitative evaluation was performed on the points-based dataset described in Section 2.2. We used the framework outlined in Olofsson et al. (2014) for our evaluation, which is based on the estimators presented in Card (1982). In contrast to the common approach of reporting confusion matrix results in terms of sample unit counts, we used an estimator to estimate the proportion of area for each cell

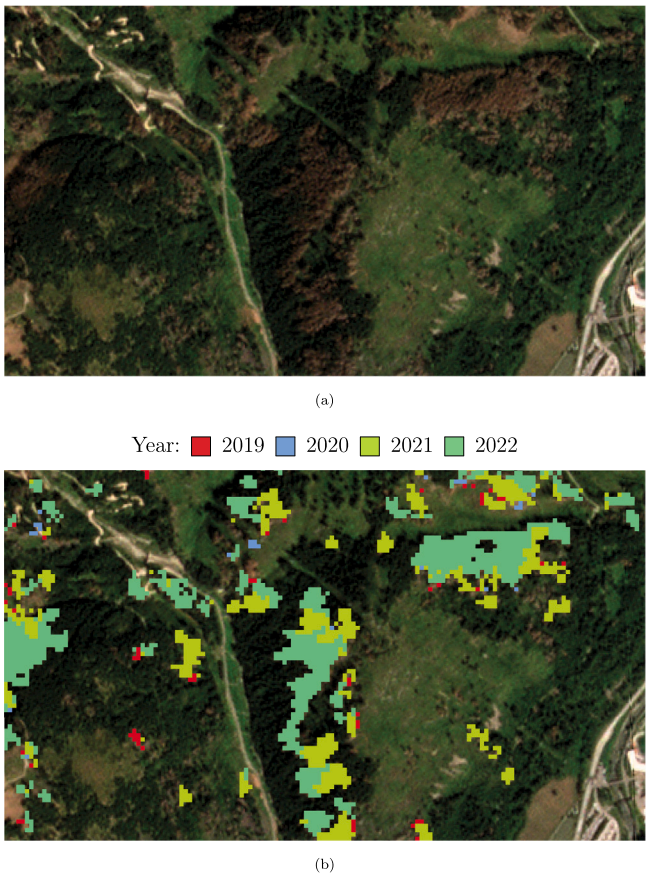

Fig. 4. Qualitative example of the method's output: (a) Planet basemap (August 2022), (b) first year of detection map.

in the confusion matrix. Specifically, we estimated the proportion of true negatives, true positives, false negatives and false positives, where negatives and positives correspond to the undisturbed and disturbed classes, respectively. It should be noted that three interpreters performed the photointerpretation in this work, which is on the lower end of the recommended number (McRoberts et al., 2018) and fewer than some studies (e.g., Powell et al., 2004). This relatively small number of interpreters can introduce bias into the estimators of proportions and of variance and standard error (McRoberts et al., 2018). For further details, including all used estimators, please refer to the Appendix and to Olofsson et al. (2014). In the following, we report the used metrics with the number referring to the specific estimator in the Appendix reported as [Eq: #]. We estimated the overall accuracy (OA), user's accuracy (UA), producer's accuracy (PA) [Eqs.: (A.1), (A.2), (A.3)] and their respective CIs [Eqs.: (A.6), (A.7), (A.8)]. Furthermore, we estimated the disturbed area (DA) of Norway spruce forests attacked by bark beetle [Eq: (A.5)], for the sampling frame of 26 000 ha, and corresponding CI [Eq: (A.9)]. For systematic sampling, the standard error estimators from which the CIs are constructed under the assumption of simple random sampling, usually overestimate the error (Olofsson et al., 2014). Consequently, the chosen sampling design has likely resulted in conservative estimates of CI.

The results of the NDVI/$TH = -0.1$ combination, which provided the largest values of accuracy metrics among all the tested combinations, were compared with the respective estimates of OA and UA, PA and area of the disturbed class of the other combinations. The comparison was performed by two-sided t-tests (alpha = 0.05) testing the null hypothesis of no significant difference between the reference estimate (NDVI/$TH = -0.1$) and the other respective estimates. In each test it

was assumed that the estimates of the two combinations that were compared, were independent. However, the compared estimates are likely correlated because the various classifications were performed on the same sample of observations. Ignoring the likely covariance between the estimates will result in inflated variances of the differences, smaller values of the test statistics and thus conservative results of the tests, i.e., rejection of fewer null hypotheses than the chosen value of alpha should indicate. On the other hand, since several tests were performed on the same dataset and we wanted to observe if the tendency of a more accurate classification of the reference combination was statistically significant, the testing problem can be characterized as simultaneous inference. When multiple tests are performed simultaneously, there will be an increased probability of erroneous rejection of the null hypotheses. A Bonferroni correction is often performed, which compensates for the increased probability of erroneous rejection by adjusting the value of alpha (Rupert, 1981). For all practical purposes, we considered that the effect of ignoring the covariances of the estimates of the compared classification combinations tended to balance the effect of ignoring the increased probability of erroneous rejection on the test statistics.

Qualitative polygon level results are presented only for the NDVI/$TH = -0.1$ combination. Three cases were considered: (1) true positive polygon (TPP) when, for a reference polygon, at least one pixel is a true positive; (2) false negative polygon (FNP) when, for a reference polygon, all corresponding pixels are false negative; (3) false positive polygon (FPP) for groups of connected pixels not included in any of the reference polygons (i.e., all pixels are false positives). We considered a polygon as TPP even with only one true positive since we are interested in modeling the capabilities of the method in predicting the location of each outbreak (Radoux and Bogaert, 2017). Such results are presented in terms of number of TPPs, FNPs, FPPs and the corresponding area statistics. To validate the timeliness of the detection, we compared the estimated date of detection (year and month) with the one obtained by photointerpretation for each true positive pixel.

4. Results

4.1. Point-based dataset quantitative results

Table 2 shows the numerical results for the point-based dataset. Overall, NDVI/$TH = -0.1$ achieved the most balanced results in terms of UA (0.91) and PA (0.81), among all index/threshold combinations. The combination MSAVI2/$TH = -0.05$ achieved a similar estimate for the PA (0.81) but a lower value for the UA (0.79). NBR/$TH = -0.02$ achieved comparable results to NDVI/$TH = -0.1$ in terms of UA but a significantly smaller value of PA. Finally, the NDRE/$TH = -0.01$ combination resulted in the smallest values of accuracy metrics, compared to the other combinations.

In terms of disturbed area, the estimates range from 1359 to 2183 ha with half-width CIs ranging from 217 to 340 ha. The NDVI/$TH = -0.1$ and MSAVI2/$TH = -0.05$ combinations provided the largest estimates. With respect to the NDVI/$TH = -0.1$ area estimate, all other indexes have at least one combination that resulted in no significant difference according to two-sided t-tests. Table 2 provides the estimated DRP, in terms of percentage, ranging from 5.3% to 8.5%.

4.2. Polygon-based dataset qualitative results

Focusing on the NDVI/$TH = -0.1$, Fig. 5 compares the distribution of the areas of all the reference polygons with the TPPs, FNPs and FPPs clearly highlighting how the last two groups are noticeably smaller (average area of 0.07 ha and 0.06 ha for FNPs and FPPs, respectively) compared to the reference average area of 0.22 ha. In terms of detection timeliness, Fig. 6 compares the year and month of detection with the reference values for all the 2578 disturbed pixels. The year difference (Fig. 6a) shows that there was agreement for 87.2% of the true positive pixels with almost all of the remaining pixels showing a ±1 year error. The month difference (Fig. 6b) is shown only the for 2247 pixels in agreement for the year of detection. The detection month of 86.9% of the 2247 pixels (75.7% of all disturbed pixels) was within ±1 month with respect to the reference value.

To further evaluate the differences between intra- and inter-annual analysis, we extended the analysis presented in Section 3.2 and Fig. 2. In details, we extracted the average temporal trajectory of all disturbed (194) and undisturbed polygons (63). We then computed the 5th percentile of all the intra- and inter-annual differences for each polygon. The distribution of the percentile values of all the undisturbed and disturbed polygons, for both the intra- and inter-annual differences, are shown in the box plots of Fig. 7.

5. Discussion

Table 2 indicates that NDVI/$TH = -0.1$ provided the largest values of UA and PA. Nevertheless, it should be noted that the accuracy metrics values of multiple combinations showed no significant difference as highlighted by the t-test. Therefore, it is not possible to definitively determine a single optimal index, in terms of accuracy metrics, based on the available results. Having said that, the literature presents conflicting findings with different works that identify various indices or spectral bands as the most effective (Hermosilla et al., 2015; Huo et al., 2021; Bárta et al., 2022; Huo et al., 2023). Hence, it could be beneficial to integrate multiple indices according to an ensemble approach, exploiting the properties of the different parts of the spectrum. Nonetheless, operational considerations should be taken into account. Unlike NBR and NDRE, which rely on 20 m resolution bands in S2 imagery, the NDVI uses NIR bands with a smaller pixel size of 10 m, providing higher native spatial detail. Additionally, the bands used for computing the NDVI are more common, compared to SWIR and red edge, in very fine spatial resolution satellite images (e.g., Planet imagery).

To better understand how well the method generalizes over the entire province of Trento, we compared the estimated DRP with the estimate of the forest service. Thus, the assumption of this statistically informal comparison was that the proportion of disturbed areas would be similar in the sampled study area and in all Norway spruce forests in the province. The estimated area of attacked Norway spruce of the forest service for the entire province by October 2022 is 9000 ha of the total 130 000 ha which roughly corresponds to 6.9% of the total area. The proportion of sample units labeled as disturbed by the photo interpreters is 5.3%. The results of Table 2 show that for 10 out of 12 combinations the DRP is in the ±1.5% range of the forest service estimate. This supports the hypothesis that the point-based dataset is well representative of the entire province. Accordingly, while we acknowledge that the dataset is not fully representative of the impact of bark beetle attacks on the entirety of Trentino's Norway spruce population, it provides a reasonable approximation from an operational standpoint. This is highlighted by Fig. 1(b) that shows how the dataset is distributed over the entire province.

The box plots of Fig. 7 confirm that the inter-annual analysis accentuates the spectral variation of disturbed areas to a greater extent than the intra-annual analysis. Moreover, when compared to the undisturbed values, inter-annual values of disturbed areas show noticeably different values whereas the intra-annual difference is closely similar to the former, strongly limiting the separability of disturbed and undisturbed areas. For undisturbed areas, no relevant difference exists between intra- and inter-annual difference values. This demonstrates that the inter-annual strategy emphasizes disturbed areas while minimizing the amplification of natural spectral variations in healthy vegetation.

Nevertheless, the inter-annual analysis can be affected by a delay or anticipation of the beginning and end of the growing season. For example, a delay in the season start can be detected as a disturbance at the beginning of the season. This is because the vegetation index of the usual growing season starting month will show smaller values

Table 2
Estimates of accuracy, disturbed area (DA) with corresponding CIs and disturbed reference proportion (DRP) of the point-based dataset for all the index/threshold combinations.

Spectral index	TH value	OA	UA		PA		Estimated DA [ha]	Estimated DRP [%]
			Undisturbed	Disturbed	Undisturbed	Disturbed		
NDVI	−0.05	0.90 ± 0.01	0.97 ± 0.01	0.35 ± 0.09	0.92 ± 0.01	0.64 ± 0.10	1660 ± 340	6.4
	−0.1	0.98 ± 0.01	0.98 ± 0.01	0.91 ± 0.08	0.99 ± 0.01	0.81 ± 0.07	2068 ± 217	8.0
	−0.2	0.96 ± 0.01	0.96 ± 0.01	0.90 ± 0.13*	0.99 ± 0.01	0.34 ± 0.07	1513 ± 276	5.9
MSAVI2	−0.05	0.97 ± 0.01*	0.98 ± 0.01	0.79 ± 0.10*	0.98 ± 0.01	0.81 ± 0.07*	2183 ± 287*	8.5
	−0.1	0.97 ± 0.01*	0.97 ± 0.01	0.92 ± 0.09*	0.99 ± 0.01	0.59 ± 0.08	1747 ± 246*	6.8
	−0.2	0.95 ± 0.01	0.95 ± 0.01	0.82 ± 0.24*	0.99 ± 0.01	0.13 ± 0.04	1359 ± 292	5.3
NBR	−0.05	0.76 ± 0.01	0.97 ± 0.01	0.12 ± 0.04	0.77 ± 0.01	0.53 ± 0.11	1407 ± 315	5.5
	−0.1	0.90 ± 0.01	0.98 ± 0.01	0.37 ± 0.08	0.91 ± 0.01	0.77 ± 0.09*	1657 ± 324	6.4
	−0.2	0.97 ± 0.01*	0.98 ± 0.01	0.87 ± 0.10*	0.99 ± 0.01	0.66 ± 0.08	1776 ± 246*	7.0
NDRE	−0.05	0.89 ± 0.01	0.98 ± 0.01	0.32 ± 0.08	0.90 ± 0.01	0.71 ± 0.09*	1574 ± 320	6.1
	−0.1	0.96 ± 0.01	0.98 ± 0.01	0.74 ± 0.12	0.98 ± 0.01	0.69 ± 0.08	1754 ± 272*	6.8
	−0.2	0.95 ± 0.01	0.96 ± 0.01	0.92 ± 0.16*	0.99 ± 0.01	0.18 ± 0.04	1394 ± 286	5.4

* Identifies the estimates (OA and UA, PA and area of the disturbed class) that according to two-sided t-tests (alpha = 0.05) are not significantly different from those of the NDVI/$TH = -0.1$ combination.

compared to the previous year. However, in the following months such false positive will no longer be detected as the index reaches its nominal values. Then, due to the intra-annual analysis, the temporal inconsistency will be eliminated. Focusing on the intra-annual analysis, the reduction of the number of false positives due to the check for temporal inconsistencies comes at the expense of a decreased sensitivity to some disturbances. The criteria defined in Section 3.2.2 are valid if the disturbance has a prolonged impact in time. This is not the case for disturbances where vegetation shows a quick recovery (e.g., after drought or frost). In these cases, the proposed method will detect the disturbance during the event. However, if in the following months the vegetation recovers sufficiently, the disturbance will no longer be detectable and will be discarded by the intra-annual analysis. Indeed, there is a trade-off between the sensitivity of the method to short-lived disturbances and to false positives. It is worth noting that full vegetation recovery usually takes from one to three years after drought (Huang et al., 2018) and frost (Vitasse et al., 2019) events. However, given the increasing risk of such events (Lamichhane, 2021), the dynamics of short-lived disturbances should be further investigated to improve their detection.

The results of Fig. 6 show that, in terms of timeliness of detection, the proposed method can achieve comparable results to the photointerpretation. It is noteworthy that both the proposed method and the photointerpretation use monthly composites, thus limiting the validation of the near real-time detection to the temporal resolution of one month. While monthly mapping represents an improvement compared to annual-scale methods, this temporal resolution may be at the upper limit of the time frame required for the planning and actuation of proactive forest management measures (Bárta et al., 2022; Huo et al., 2021). Imagery with a shorter revisit interval, such as the harmonized S2 and Landsat datasets like HLS (Claverie et al., 2018) and Sen2Like (Saunier et al., 2022) could be used to improve the temporal resolution. However, this comes at the expense of a degradation of the S2 resolution to 30 m in HLS or the upscaling of Landsat data in Sen2Like. Another improvement could be a hierarchical approach where, after the proposed method has estimated the year and month of detection, the individual images of the period of interest are analyzed searching for the first image where the attack is detectable.

6. Conclusion

The analysis of multispectral time series data in the form of monthly composites enables the mapping of historical and recent NSRD with sub-annual temporal resolution. The proposed method has the potential to provide a continuous and near real-time mapping of disturbances. This is made possible by leveraging both inter- and intra-annual analysis. The former analyzes inter-annual temporal trends, while the latter

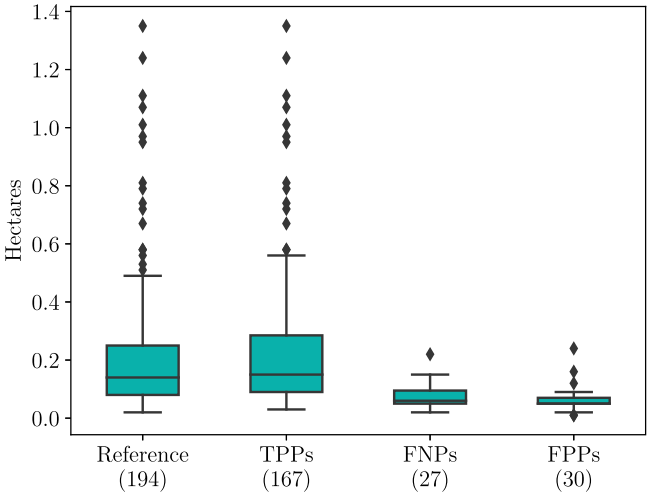

Fig. 5. Box plots of the areas of the reference, true positive (TPPs), false negatives (FNPs) and false positives (FPPs) polygons obtained with NDVI/$TH = -0.1$. The number of polygons of each category is show in brackets on the x axis.

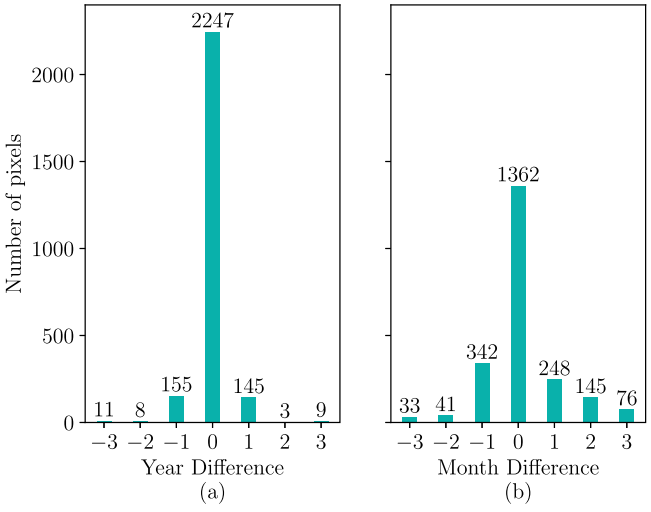

Fig. 6. Difference between the estimated and reference detection dates (year and month) for all the true positive pixels in terms of year and month. The month difference is computed only for the 2247 pixels where estimated and reference year corresponds.

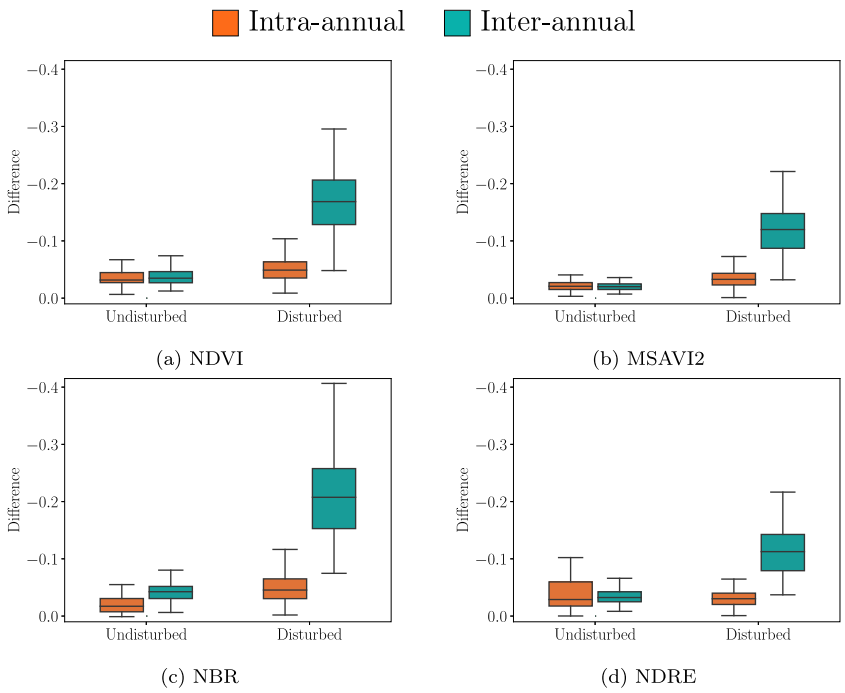

Fig. 7. Box plots comparing intra- and inter-annual difference values for undisturbed and disturbed areas. The Y-axes are inverted.

enables mapping at a sub-annual temporal resolution and the removal of temporal inconsistencies. This conclusion is supported by the quantitative results obtained from the point-based dataset. Furthermore, the qualitative results of the polygon-based dataset demonstrate that the method can achieve comparable results to manual photointerpretation in terms of timeliness of detection. From an operational standpoint, the method detected 86.1% of the individual attacks.

The continuous and near real-time mapping of this method enhances the characterization of temporal dynamics of NSRD. This knowledge and the use of the method in an operational scenario could assist forest managers in implementing management practices to improve resilience and response strategies to effectively react to changes. Future studies should focus on further improving the temporal resolution and to better understand how early NSRD effects can be predicted from spaceborne sensors.

CRediT authorship contribution statement

Daniele Marinelli: Conceptualization, Methodology, Software, Validation, Visualization, Writing – original draft, Writing – review & editing. **Michele Dalponte:** Conceptualization, Methodology, Validation, Writing – review & editing. **Lorenzo Frizzera:** Validation, Data curation. **Erik Næsset:** Validation, Writing – review & editing. **Damiano Gianelle:** Supervision, Conceptualization, Writing – review & editing.

Declaration of competing interest

The authors declare that they have no known competing financial interests or personal relationships that could have appeared to influence the work reported in this paper.

Data availability

The Sentinel-2 data are publicly available. The validation datasets used in this work are at available at doi.org/10.5281/zenodo.8426109.

Declaration of Generative AI and AI-assisted technologies in the writing process

During the preparation of this work the authors used ChatGPT in order to improve readability. After using this tool, the authors reviewed and edited the content as needed and take full responsibility for the content of the publication.

Acknowledgments

This work was funded by the Highlander project co-financed by the Connecting Europe Facility of the European Union (Grant agreement n INEA/CEF/ICT/A2018/1815462). The authors would like to thank the forest service of the Province of Trento for the collaboration and providing part of the data used in this work.

Appendix. Accuracy Estimators

In this section, the estimators used for the accuracy metrics and areas are provided. Let u and d be the undisturbed and disturbed classes, respectively. Let A_{tot} be the total area (26 000 ha in this work) and W_u and W_d be the proportions of area mapped as undisturbed and disturbed, respectively. The confusion matrix can be reported in terms of sample units count (Table A.1a) and area proportion (Table A.1b). n_{ij}, with $(i, j) \in \{u, d\}$, is the counts of sample units with map class i and reference class j with i and j representing the rows and columns of the confusion matrix, respectively. The same notation is used for the area proportion p_{ij}. The overall accuracy (OA), user's accuracy (UA) of map class i and producer's accuracy (PA) of reference class j are:

$$\mathrm{OA} = \sum_{j \in \{u,d\}} p_{jj}, \tag{A.1}$$

$$\mathrm{UA}_i = \frac{p_{ii}}{p_{i\cdot}}, \tag{A.2}$$

$$\mathrm{PA}_j = \frac{p_{jj}}{p_{\cdot j}}, \tag{A.3}$$

respectively. The poststratified estimator of p_{ij} used in this work is:

$$\hat{p}_{ij} = W_i \frac{n_{ij}}{n_{i\cdot}}. \tag{A.4}$$

Table A.1
Confusion matrix reported in terms of sample units count (a) or area proportion (b).

(a) Sample units count				
		Reference		
		$Class_u$	$Class_d$	Total
Map	$Class_u$	n_{uu}	n_{ud}	$n_{u\cdot}$
	$Class_d$	n_{du}	n_{dd}	$n_{d\cdot}$
	Total	$n_{\cdot u}$	$n_{\cdot d}$	
(b) Area proportion				
		Reference		
		$Class_u$	$Class_d$	Total
Map	$Class_u$	p_{uu}	p_{ud}	$p_{u\cdot} = \sum_{j\in\{u,d\}} p_{uj}$
	$Class_d$	p_{du}	p_{dd}	$p_{d\cdot} = \sum_{j\in\{u,d\}} p_{dj}$
	Total	$p_{\cdot u} = \sum_{i\in\{u,d\}} p_{iu}$	$p_{\cdot d} = \sum_{i\in\{u,d\}} p_{id}$	

The estimated area of class j is:

$$\hat{A}_j = A_{tot} \times \hat{p}_{\cdot j}. \tag{A.5}$$

Since $\hat{p}_{ij}$ is an estimate, this is the case also for the reported accuracy metrics. Accordingly, CIs are provided. These are computed as $\pm 1.96\sqrt{V(x)}$ where $V(x)$ is the variance of metric x. The variance of OA is estimated as:

$$\hat{V}(\hat{\mathrm{OA}}) = \sum_{i\in\{u,d\}} W_i^2 \hat{\mathrm{UA}}_i(1-\hat{\mathrm{UA}}_i)/(n_{i\cdot}-1) \tag{A.6}$$

The variance of UA of map class i is estimated as:

$$\hat{V}(\hat{\mathrm{UA}}_i) = \hat{\mathrm{UA}}_i(1-\hat{\mathrm{UA}}_i)/(n_{i\cdot}-1) \tag{A.7}$$

The variance of PA of reference class j is estimated as:

$$\hat{V}(\hat{\mathrm{PA}}_j) = \frac{1}{\hat{N}_{\cdot j}^2}\left[\frac{N_{j\cdot}^2(1-\hat{\mathrm{PA}}_j)^2\hat{\mathrm{UA}}_j(1-\hat{\mathrm{UA}}_j)}{n_{j\cdot}-1} + \hat{\mathrm{PA}}_j^2 \sum_{i\in\{u,d\}, i\neq j} N_{i\cdot}^2 \frac{n_{ij}}{n_{i\cdot}}\left(1-\frac{n_{ij}}{n_{i\cdot}}\right)/(n_{i\cdot}-1)\right] \tag{A.8}$$

where $\hat{N}_{\cdot j} = \sum_{i\in\{u,d\}} \frac{N_{i\cdot}}{n_{i\cdot}} n_{ij}$ is the estimated marginal total pixel counts of reference class j. $N_{i\cdot}$ is the total number of pixels of map class i. Finally, the standard error for the area proportion estimator is:

$$S(\hat{p}_{\cdot j}) = \sqrt{\sum_{i\in\{u,d\}} \frac{W_i\hat{p}_{ij} - \hat{p}_{ij}^2}{n_{i\cdot}-1}} \tag{A.9}$$

The CI of the area estimates of class j is $1.96 \times A_{tot} \times S(\hat{p}_{\cdot j})$.

References

Bárta, V., Hanuš, J., Dobrovolný, L., Homolová, L., 2022. Comparison of field survey and remote sensing techniques for detection of bark beetle-infested trees. Forest Ecol. Manag. 506, 119984. http://dx.doi.org/10.1016/j.foreco.2021.119984.

Bertoluzza, M., Bruzzone, L., Bovolo, F., 2017. A novel framework for bi-temporal change detection in image time series. In: 2017 IEEE International Geoscience and Remote Sensing Symposium (IGARSS). pp. 1087–1090. http://dx.doi.org/10.1109/IGARSS.2017.8127145.

Bovolo, F., Bruzzone, L., 2015. The time variable in data fusion: A change detection perspective. IEEE Geosci. Remote Sens. Mag. 3 (3), 8–26. http://dx.doi.org/10.1109/MGRS.2015.2443494.

Brecka, A.F., Shahi, C., Chen, H.Y., 2018. Climate change impacts on boreal forest timber supply. For. Policy Econ. 92, 11–21. http://dx.doi.org/10.1016/j.forpol.2018.03.010.

Bruzzone, L., Bovolo, F., 2014. A novel circular approach to change detection in pair of images extracted from image time series. In: 2014 IEEE Geoscience and Remote Sensing Symposium. pp. 1140–1143. http://dx.doi.org/10.1109/IGARSS.2014.6946631.

Card, D., 1982. Using known map category marginal frequencies to improve estimates of thematic map accuracy. Photogramm. Eng. Remote Sens. 48 (3), 431–439.

Cavalli, A., Francini, S., McRoberts, R.E., Falanga, V., Congedo, L., De Fioravante, P., Maesano, M., Munafò, M., Chirici, G., Scarascia Mugnozza, G., 2023. Estimating afforestation area using landsat time series and photointerpreted datasets. Remote Sens. 15 (4), http://dx.doi.org/10.3390/rs15040923.

Claverie, M., Ju, J., Masek, J.G., Dungan, J.L., Vermote, E.F., Roger, J.-C., Skakun, S.V., Justice, C., 2018. The Harmonized Landsat and Sentinel-2 surface reflectance data set. Remote Sens. Environ. 219, 145–161. http://dx.doi.org/10.1016/j.rse.2018.09.002.

Coops, N.C., Johnson, M., Wulder, M.A., White, J.C., 2006. Assessment of QuickBird high spatial resolution imagery to detect red attack damage due to mountain pine beetle infestation. Remote Sens. Environ. 103 (1), 67–80. http://dx.doi.org/10.1016/j.rse.2006.03.012.

Coops, N.C., Shang, C., Wulder, M.A., White, J.C., Hermosilla, T., 2020. Change in forest condition: Characterizing non-stand replacing disturbances using time series satellite imagery. Forest Ecol. Manag. 474, 118370. http://dx.doi.org/10.1016/j.foreco.2020.118370.

Coops, N.C., Wulder, M.A., White, J.C., et al., 2007. Identifying and describing forest disturbance and spatial pattern: data selection issues and methodological implications. In: Forest Disturbance and Spatial Pattern: Remote Sensing and GIS Approaches. Citeseer, p. 264.

Eitel, J.U., Vierling, L.A., Litvak, M.E., Long, D.S., Schulthess, U., Ager, A.A., Krofcheck, D.J., Stoscheck, L., 2011. Broadband, red-edge information from satellites improves early stress detection in a New Mexico conifer woodland. Remote Sens. Environ. 115 (12), 3640–3646. http://dx.doi.org/10.1016/j.rse.2011.09.002.

Francini, S., Cavalli, A., D'Amico, G., McRoberts, R.E., Maesano, M., Munafò, M., Scarascia Mugnozza, G., Chirici, G., 2023. Reusing remote sensing-based validation data: Comparing direct and indirect approaches for afforestation monitoring. Remote Sens. 15 (6), http://dx.doi.org/10.3390/rs15061638.

Francini, S., McRoberts, R.E., D'Amico, G., Coops, N.C., Hermosilla, T., White, J.C., Wulder, M.A., Marchetti, M., Mugnozza, G.S., Chirici, G., 2022. An open science and open data approach for the statistically robust estimation of forest disturbance areas. Int. J. Appl. Earth Obs. Geoinf. 106, 102663. http://dx.doi.org/10.1016/j.jag.2021.102663.

Francini, S., McRoberts, R.E., Giannetti, F., Marchetti, M., Mugnozza, G.S., Chirici, G., 2021. The Three Indices Three Dimensions (3I3D) algorithm: a new method for forest disturbance mapping and area estimation based on optical remotely sensed imagery. Int. J. Remote Sens. 42 (12), 4693–4711. http://dx.doi.org/10.1080/01431161.2021.1899334.

Frolking, S., Palace, M.W., Clark, D.B., Chambers, J.Q., Shugart, H.H., Hurtt, G.C., 2009. Forest disturbance and recovery: A general review in the context of spaceborne remote sensing of impacts on aboveground biomass and canopy structure. J. Geophys. Res.: Biogeosci. 114 (G2), http://dx.doi.org/10.1029/2008JG000911.

Gao, Y., Skutsch, M., Paneque-Gálvez, J., Ghilardi, A., 2020. Remote sensing of forest degradation: a review. Environ. Res. Lett. 15 (10), 103001. http://dx.doi.org/10.1088/1748-9326/abaad7.

Giannetti, F., Pegna, R., Francini, S., McRoberts, R.E., Travaglini, D., Marchetti, M., Scarascia Mugnozza, G., Chirici, G., 2020. A new method for automated clearcut disturbance detection in mediterranean coppice forests using landsat time series. Remote Sens. 12 (22), http://dx.doi.org/10.3390/rs12223720.

Giovannini, L., Davolio, S., Zaramella, M., Zardi, D., Borga, M., 2021. Multi-model convection-resolving simulations of the October 2018 Vaia storm over Northeastern Italy. Atmos. Res. 253, 105455. http://dx.doi.org/10.1016/j.atmosres.2021.105455.

Gong, W., Huang, C., Houghton, R.A., Nassikas, A., Zhao, F., Tao, X., Lu, J., Schleeweis, K., 2022. Carbon fluxes from contemporary forest disturbances in North Carolina evaluated using a grid-based carbon accounting model and fine resolution remote sensing products. Sci. Remote Sens. 5, 100042. http://dx.doi.org/10.1016/j.srs.2022.100042.

Hermosilla, T., Wulder, M.A., White, J.C., Coops, N.C., 2019. Prevalence of multiple forest disturbances and impact on vegetation regrowth from interannual Landsat time series (1985–2015). Remote Sens. Environ. 233, 111403. http://dx.doi.org/10.1016/j.rse.2019.111403.

Hermosilla, T., Wulder, M.A., White, J.C., Coops, N.C., Hobart, G.W., 2015. Regional detection, characterization, and attribution of annual forest change from 1984 to 2012 using Landsat-derived time-series metrics. Remote Sens. Environ. 170, 121–132. http://dx.doi.org/10.1016/j.rse.2015.09.004.

Hirsch, A.I., Little, W.S., Houghton, R.A., Scott, N.A., White, J.D., 2004. The net carbon flux due to deforestation and forest re-growth in the Brazilian Amazon: Analysis using a process-based model. Global Change Biol. 10 (5), 908–924. http://dx.doi.org/10.1111/j.1529-8817.2003.00765.x.

Hlásny, T., Krokene, P., Liebhold, A., Montagné-Huck, C., Müller, J., Qin, H., Raffa, K., Schelhaas, M., Seidl, R., Svoboda, M., Viiri, H., 2019. Living with bark beetles: impacts, outlook and management options. In: From Science to Policy, Number 8, European Forest Institute, http://dx.doi.org/10.36333/fs08.

Huang, M., Wang, X., Keenan, T.F., Piao, S., 2018. Drought timing influences the legacy of tree growth recovery. Global Change Biol. 24 (8), 3546–3559. http://dx.doi.org/10.1111/gcb.14294.

Huo, L., Lindberg, E., Bohlin, J., Persson, H.J., 2023. Assessing the detectability of European spruce bark beetle green attack in multispectral drone images with high spatial- and temporal resolutions. Remote Sens. Environ. 287, 113484. http://dx.doi.org/10.1016/j.rse.2023.113484.

Huo, L., Persson, H.J., Lindberg, E., 2021. Early detection of forest stress from European spruce bark beetle attack, and a new vegetation index: Normalized distance red & SWIR (NDRS). Remote Sens. Environ. 255, 112240. http://dx.doi.org/10.1016/j.rse.2020.112240.

Kennedy, R.E., Yang, Z., Cohen, W.B., 2010. Detecting trends in forest disturbance and recovery using yearly Landsat time series: 1. LandTrendr — Temporal segmentation algorithms. Remote Sens. Environ. 114 (12), 2897–2910. http://dx.doi.org/10.1016/j.rse.2010.07.008.

Kennedy, R.E., Yang, Z., Cohen, W.B., Pfaff, E., Braaten, J., Nelson, P., 2012. Spatial and temporal patterns of forest disturbance and regrowth within the area of the Northwest Forest Plan. Remote Sens. Environ. 122, 117–133. http://dx.doi.org/10.1016/j.rse.2011.09.024, Landsat Legacy Special Issue.

Kurz, W.A., Dymond, C., Stinson, G., Rampley, G., Neilson, E., Carroll, A., Ebata, T., Safranyik, L., 2008. Mountain pine beetle and forest carbon feedback to climate change. Nature 452 (7190), 987–990. http://dx.doi.org/10.1038/nature06777.

Kurz, W., Dymond, C., White, T., Stinson, G., Shaw, C., Rampley, G., Smyth, C., Simpson, B., Neilson, E., Trofymow, J., Metsaranta, J., Apps, M., 2009. CBM-CFS3: A model of carbon-dynamics in forestry and land-use change implementing IPCC standards. Ecol. Model. 220 (4), 480–504. http://dx.doi.org/10.1016/j.ecolmodel.2008.10.018.

Lamichhane, J.R., 2021. Rising risks of late-spring frosts in a changing climate. Nature Clim. Change 11 (7), 554–555. http://dx.doi.org/10.1038/s41558-021-01090-x.

Lima, T.A., Beuchle, R., Langner, A., Grecchi, R.C., Griess, V.C., Achard, F., 2019. Comparing Sentinel-2 MSI and Landsat 8 OLI imagery for monitoring selective logging in the Brazilian Amazon. Remote Sens. 11 (8), http://dx.doi.org/10.3390/rs11080961.

Liu, S., Bond-Lamberty, B., Hicke, J.A., Vargas, R., Zhao, S., Chen, J., Edburg, S.L., Hu, Y., Liu, J., McGuire, A.D., Xiao, J., Keane, R., Yuan, W., Tang, J., Luo, Y., Potter, C., Oeding, J., 2011. Simulating the impacts of disturbances on forest carbon cycling in North America: Processes, data, models, and challenges. J. Geophys. Res.: Biogeosci. 116 (G4), http://dx.doi.org/10.1029/2010JG001585.

Löw, M., Koukal, T., 2020. Phenology modelling and forest disturbance mapping with sentinel-2 time series in austria. Remote Sens. 12 (24), 4191. http://dx.doi.org/10.3390/rs12244191.

Matricardi, E.A., Skole, D.L., Pedlowski, M.A., Chomentowski, W., 2013. Assessment of forest disturbances by selective logging and forest fires in the Brazilian Amazon using Landsat data. Int. J. Remote Sens. 34 (4), 1057–1086. http://dx.doi.org/10.1080/01431161.2012.717182.

McRoberts, R.E., Stehman, S.V., Liknes, G.C., Næsset, E., Sannier, C., Walters, B.F., 2018. The effects of imperfect reference data on remote sensing-assisted estimators of land cover class proportions. ISPRS J. Photogramm. Remote Sens. 142, 292–300. http://dx.doi.org/10.1016/j.isprsjprs.2018.06.002.

Mulverhill, C., Coops, N.C., Achim, A., 2023. Continuous monitoring and sub-annual change detection in high-latitude forests using Harmonized Landsat Sentinel-2 data. ISPRS J. Photogramm. Remote Sens. 197, 309–319. http://dx.doi.org/10.1016/j.isprsjprs.2023.02.002.

Olofsson, P., Foody, G.M., Herold, M., Stehman, S.V., Woodcock, C.E., Wulder, M.A., 2014. Good practices for estimating area and assessing accuracy of land change. Remote Sens. Environ. 148, 42–57. http://dx.doi.org/10.1016/j.rse.2014.02.015.

Paris, C., Weikmann, G., Bruzzone, L., 2020. Monitoring of agricultural areas by using Sentinel 2 image time series and deep learning techniques. In: Bruzzone, L., Bovolo, F., Santi, E. (Eds.), Image and Signal Processing for Remote Sensing XXVI, Vol. 11533. International Society for Optics and Photonics. SPIE, p. 115330K. http://dx.doi.org/10.1117/12.2574745.

Planet Team, 2017–. Planet Application Program Interface: In Space for Life on Earth. Planet, URL: https://www.planet.com/products/basemap/.

Powell, R., Matzke, N., de Souza, C., Clark, M., Numata, I., Hess, L., Roberts, D., 2004. Sources of error in accuracy assessment of thematic land-cover maps in the Brazilian Amazon. Remote Sens. Environ. 90 (2), 221–234. http://dx.doi.org/10.1016/j.rse.2003.12.007.

Radoux, J., Bogaert, P., 2017. Good practices for object-based accuracy assessment. Remote Sens. 9 (7), http://dx.doi.org/10.3390/rs9070646.

Rodeghiero, M., Tonolli, S., Vescovo, L., Gianelle, D., Cescatti, A., Sottocornola, M., 2010. INFOCARB: A regional scale forest carbon inventory (Provincia Autonoma di Trento, Southern Italian Alps). Forest Ecol. Manag. 259 (6), 1093–1101. http://dx.doi.org/10.1016/j.foreco.2009.12.019.

Rupert, G.M., 1981. Simultaneous Statistical Inference, second ed. Springer, New York, http://dx.doi.org/10.1007/978-1-4613-8122-8.

Saunier, S., Pflug, B., Lobos, I.M., Franch, B., Louis, J., De Los Reyes, R., Debaecker, V., Cadau, E.G., Boccia, V., Gascon, F., Kocaman, S., 2022. Sen2Like: Paving the way towards harmonization and fusion of optical data. Remote Sens. 14 (16), http://dx.doi.org/10.3390/rs14163855.

Seidl, R., Schelhaas, M.-j., Lexer, M.J., 2011. Unraveling the drivers of intensifying forest disturbance regimes in Europe. Global Change Biol. 17 (9), 2842–2852. http://dx.doi.org/10.1111/j.1365-2486.2011.02452.x.

Seidl, R., Thom, D., Kautz, M., Martin-Benito, D., Peltoniemi, M., Vacchiano, G., Wild, J., Ascoli, D., Petr, M., Honkaniemi, J., et al., 2017. Forest disturbances under climate change. Nat. Clim. Change 7 (6), 395–402. http://dx.doi.org/10.1038/nclimate3303.

Senf, C., Seidl, R., 2021. Mapping the forest disturbance regimes of Europe. Nat. Sustain. 4 (1), 63–70. http://dx.doi.org/10.1038/s41893-020-00609-y.

Skakun, S., Wevers, J., Brockmann, C., Doxani, G., Aleksandrov, M., Batič, M., Frantz, D., Gascon, F., Gómez-Chova, L., Hagolle, O., López-Puigdollers, D., Louis, J., Lubej, M., Mateo-García, G., Osman, J., Peressutti, D., Pflug, B., Puc, J., Richter, R., Roger, J.-C., Scaramuzza, P., Vermote, E., Vesel, N., Zupanc, A., Žust, L., 2022. Cloud Mask Intercomparison eXercise (CMIX): An evaluation of cloud masking algorithms for Landsat 8 and Sentinel-2. Remote Sens. Environ. 274, 112990. http://dx.doi.org/10.1016/j.rse.2022.112990.

Turner, W., Rondinini, C., Pettorelli, N., Mora, B., Leidner, A., Szantoi, Z., Buchanan, G., Dech, S., Dwyer, J., Herold, M., Koh, L., Leimgruber, P., Taubenboeck, H., Wegmann, M., Wikelski, M., Woodcock, C., 2015. Free and open-access satellite data are key to biodiversity conservation. Biol. Cons. 182, 173–176. http://dx.doi.org/10.1016/j.biocon.2014.11.048.

Tyukavina, A., Hansen, M.C., Potapov, P.V., Stehman, S.V., Smith-Rodriguez, K., Okpa, C., Aguilar, R., 2017. Types and rates of forest disturbance in Brazilian Legal Amazon, 2000–2013. Sci. Adv. 3 (4), e1601047. http://dx.doi.org/10.1126/sciadv.1601047.

Verbesselt, J., Hyndman, R., Zeileis, A., Culvenor, D., 2010. Phenological change detection while accounting for abrupt and gradual trends in satellite image time series. Remote Sens. Environ. 114 (12), 2970–2980. http://dx.doi.org/10.1016/j.rse.2010.08.003.

Vitasse, Y., Bottero, A., Cailleret, M., Bigler, C., Fonti, P., Gessler, A., Lévesque, M., Rohner, B., Weber, P., Rigling, A., Wohlgemuth, T., 2019. Contrasting resistance and resilience to extreme drought and late spring frost in five major European tree species. Global Change Biol. 25 (11), 3781–3792. http://dx.doi.org/10.1111/gcb.14803.

Waterworth, R., Richards, G., 2008. Implementing Australian forest management practices into a full carbon accounting model. Forest Ecol. Manag. 255 (7), 2434–2443. http://dx.doi.org/10.1016/j.foreco.2008.01.004.

White, J.C., Wulder, M.A., Hermosilla, T., Coops, N.C., Hobart, G.W., 2017. A nationwide annual characterization of 25years of forest disturbance and recovery for Canada using Landsat time series. Remote Sens. Environ. 194, 303–321. http://dx.doi.org/10.1016/j.rse.2017.03.035.

White, J.C., Wulder, M.A., Hobart, G.W., Luther, J.E., Hermosilla, T., Griffiths, P., Coops, N.C., Hall, R.J., Hostert, P., Dyk, A., Guindon, L., 2014. Pixel-based image compositing for large-area dense time series applications and science. Can. J. Remote Sens. 40 (3), 192–212. http://dx.doi.org/10.1080/07038992.2014.945827.

Wulder, M.A., Loveland, T.R., Roy, D.P., Crawford, C.J., Masek, J.G., Woodcock, C.E., Allen, R.G., Anderson, M.C., Belward, A.S., Cohen, W.B., Dwyer, J., Erb, A., Gao, F., Griffiths, P., Helder, D., Hermosilla, T., Hipple, J.D., Hostert, P., Hughes, M.J., Huntington, J., Johnson, D.M., Kennedy, R., Kilic, A., Li, Z., Lymburner, L., McCorkel, J., Pahlevan, N., Scambos, T.A., Schaaf, C., Schott, J.R., Sheng, Y., Storey, J., Vermote, E., Vogelmann, J., White, J.C., Wynne, R.H., Zhu, Z., 2019. Current status of Landsat program, science, and applications. Remote Sens. Environ. 225, 127–147. http://dx.doi.org/10.1016/j.rse.2019.02.015.

Zanetti, M., Saha, S., Marinelli, D., Magliozzi, M.L., Zavagli, M., Costantini, M., Bovolo, F., Bruzzone, L., 2022. A system for burned area detection on multispectral imagery. IEEE Trans. Geosci. Remote Sens. 60, 1–15. http://dx.doi.org/10.1109/TGRS.2021.3110280.

Zhang, Y., Ling, F., Wang, X., Foody, G.M., Boyd, D.S., Li, X., Du, Y., Atkinson, P.M., 2021. Tracking small-scale tropical forest disturbances: Fusing the Landsat and Sentinel-2 data record. Remote Sens. Environ. 261, 112470. http://dx.doi.org/10.1016/j.rse.2021.112470.

Zhu, Z., Woodcock, C.E., 2014. Continuous change detection and classification of land cover using all available Landsat data. Remote Sens. Environ. 144, 152–171. http://dx.doi.org/10.1016/j.rse.2014.01.011.